

# UC Berkeley

## UC Berkeley Previously Published Works

### Title

High-throughput screening of hypothetical metal-organic frameworks for thermal conductivity

### Permalink

<https://escholarship.org/uc/item/60x2k1tv>

### Journal

npj Computational Materials, 9(1)

### ISSN

2057-3960

### Authors

Islamov, Meirbek

Babaei, Hasan

Anderson, Ryther

et al.

### Publication Date

2023

### DOI

10.1038/s41524-022-00961-x

### Copyright Information

This work is made available under the terms of a Creative Commons Attribution License, available at <https://creativecommons.org/licenses/by/4.0/>

Peer reviewed

## ARTICLE OPEN



# High-throughput screening of hypothetical metal-organic frameworks for thermal conductivity

Meiirbek Islamov<sup>1</sup>, Hasan Babaei<sup>2</sup>✉, Ryther Anderson<sup>3</sup>, Kutay B. Sezginel<sup>1</sup>, Jeffrey R. Long<sup>2,4,5</sup>, Alan J. H. McGaughey<sup>6</sup>, Diego A. Gomez-Gualdrón<sup>3</sup> and Christopher E. Wilmer<sup>1,7</sup>✉

Thermal energy management in metal-organic frameworks (MOFs) is an important, yet often neglected, challenge for many adsorption-based applications such as gas storage and separations. Despite its importance, there is insufficient understanding of the structure-property relationships governing thermal transport in MOFs. To provide a data-driven perspective into these relationships, here we perform large-scale computational screening of thermal conductivity  $k$  in MOFs, leveraging classical molecular dynamics simulations and 10,194 hypothetical MOFs created using the ToBaCCo 3.0 code. We found that high thermal conductivity in MOFs is favored by high densities ( $> 1.0 \text{ g cm}^{-3}$ ), small pores ( $< 10 \text{ \AA}$ ), and four-connected metal nodes. We also found that 36 MOFs exhibit ultra-low thermal conductivity ( $< 0.02 \text{ W m}^{-1} \text{ K}^{-1}$ ), which is primarily due to having extremely large pores ( $\sim 65 \text{ \AA}$ ). Furthermore, we discovered six hypothetical MOFs with very high thermal conductivity ( $> 10 \text{ W m}^{-1} \text{ K}^{-1}$ ), the structures of which we describe in additional detail.

npj Computational Materials (2023)9:11; <https://doi.org/10.1038/s41524-022-00961-x>

## INTRODUCTION

Metal-organic frameworks (MOFs) are crystalline materials with nanoscopic pores that self-assemble from constituent building blocks (inorganic metal nodes and organic linkers)<sup>1,2</sup> and have attracted significant interest for a diverse range of applications, from gas storage<sup>3–8</sup>, chemical separations<sup>9–11</sup>, sensing<sup>12–14</sup>, catalysis<sup>15–17</sup>, drug-delivery<sup>18–20</sup>, to thermoelectrics<sup>21–25</sup>. Primarily, it is their exceptional tunability and high internal surface areas that have made MOFs candidates for such a wide range of applications<sup>26,27</sup>. However, a property that needs consideration in practical applications of MOFs is thermal conductivity  $k$ <sup>28</sup>. For instance, in adsorptive gas storage applications, the exothermicity of gas adsorption can generate a significant amount of heat that, if not dissipated rapidly, could unduly raise the temperature and reduce MOF adsorption capacity<sup>29</sup>. In catalytic applications, temperature control is also critical, in which case MOFs with high thermal conductivity could mitigate undesirable temperature gradients. On the other hand, in thermoelectric applications MOFs with low thermal conductivities would be favored, as the figure of merit  $ZT$  is inversely related to  $k$ <sup>21–25</sup>.

In the past few years, thermal transport properties of MOFs have received more attention<sup>30–43</sup>. Recent studies have considered the influence of pore size and shape<sup>37</sup>, interpenetration<sup>38</sup>, defects<sup>39</sup>, the presence of adsorbates<sup>36,40,41</sup>, chemical functionalization<sup>42</sup>, and node-linker bonding interactions<sup>43</sup> on the thermal conductivity of MOFs.

To date, MOFs have typically been found to have low thermal conductivities ( $< 2 \text{ W m}^{-1} \text{ K}^{-1}$ )<sup>39</sup>. The highly porous nature and low density of MOFs inhibit the efficient transport of phonons. Additionally, the high chemical diversity of MOFs makes them prone to atomic mass mismatches and dissimilarity in bond stiffnesses within their structures, which has been found to

increase phonon scattering<sup>36</sup>. To date, experimentally measured thermal conductivities of the more commonly known MOFs include values such as  $0.32 \text{ W m}^{-1} \text{ K}^{-1}$  (IRMOF-1 single crystals)<sup>31</sup>,  $0.11 \text{ W m}^{-1} \text{ K}^{-1}$  (UiO-66 powders)<sup>44</sup>,  $0.19 \text{ W m}^{-1} \text{ K}^{-1}$  (UiO-67 powders)<sup>44</sup>,  $0.39 \text{ W m}^{-1} \text{ K}^{-1}$  (Cu-BTC powders)<sup>44</sup>,  $0.26 \text{ W m}^{-1} \text{ K}^{-1}$  (HKUST-1 microcrystals)<sup>45</sup>,  $0.44\text{--}0.73 \text{ W m}^{-1} \text{ K}^{-1}$  (HKUST-1 single crystals and thin films)<sup>36</sup>,  $0.32 \text{ W m}^{-1} \text{ K}^{-1}$  (ZIF-8 thin films)<sup>46</sup>, and  $1.3 \text{ W m}^{-1} \text{ K}^{-1}$  (perovskite-like MOF-1 single crystals)<sup>47</sup>. Experimentally measuring the intrinsic thermal conductivity of a MOF single crystal, as opposed to the system thermal conductivity of a packed powder bed, can be rather challenging. This is because measured thermal conductivity values are strongly affected by interfaces, grain boundaries, and inter-particle void spaces, making it difficult to ascertain the intrinsic heat transfer mechanisms within the bulk crystal, as well as to relate the observed thermal transport behavior to the MOF structure or chemical composition<sup>36</sup>.

In this regard, classical molecular dynamics (MD) can be a particularly useful tool for obtaining the bulk crystalline thermal conductivities of MOFs. Previously, MD simulations have been used to calculate the thermal conductivities of MOF-5 (also known as IRMOF-1)<sup>30</sup>, HKUST-1<sup>36,39,40</sup>,  $\text{M}_2(\text{dobpdc})$ <sup>41</sup>, and a number of zeolitic imidazolate frameworks (ZIFs)<sup>42,48</sup>. Between inaccuracies in the simulation force fields and the numerous factors confounding experimental thermal conductivity measurements, it is difficult to validate the absolute value of  $k$  predicted or measured by either simulations or experiments. However, simulations are useful for investigating trends, intrinsic heat transfer mechanisms, and structure-property relationships. For instance, earlier computational studies showed that MOF thermal conductivity decreases when the pore size<sup>37,48</sup>, linker length<sup>49</sup>, or defect concentration increases<sup>39</sup>.

<sup>1</sup>Department of Chemical & Petroleum Engineering, University of Pittsburgh, Pittsburgh, PA 15261, USA. <sup>2</sup>Department of Chemistry, University of California, Berkeley, Berkeley, CA 94720, USA. <sup>3</sup>Department of Chemical and Biological Engineering, Colorado School of Mines, Golden, CO 80401, USA. <sup>4</sup>Department of Chemical and Biomolecular Engineering, University of California, Berkeley, Berkeley, CA 94720, USA. <sup>5</sup>Materials Sciences Division, Lawrence Berkeley National Laboratory, Berkeley, CA 94720, USA. <sup>6</sup>Department of Mechanical Engineering, Carnegie Mellon University, Pittsburgh, PA 15213, USA. <sup>7</sup>Department of Electrical & Computer Engineering, University of Pittsburgh, Pittsburgh, PA 15261, USA. ✉email: hnbabaei@gmail.com; c.wilmer@gmail.com

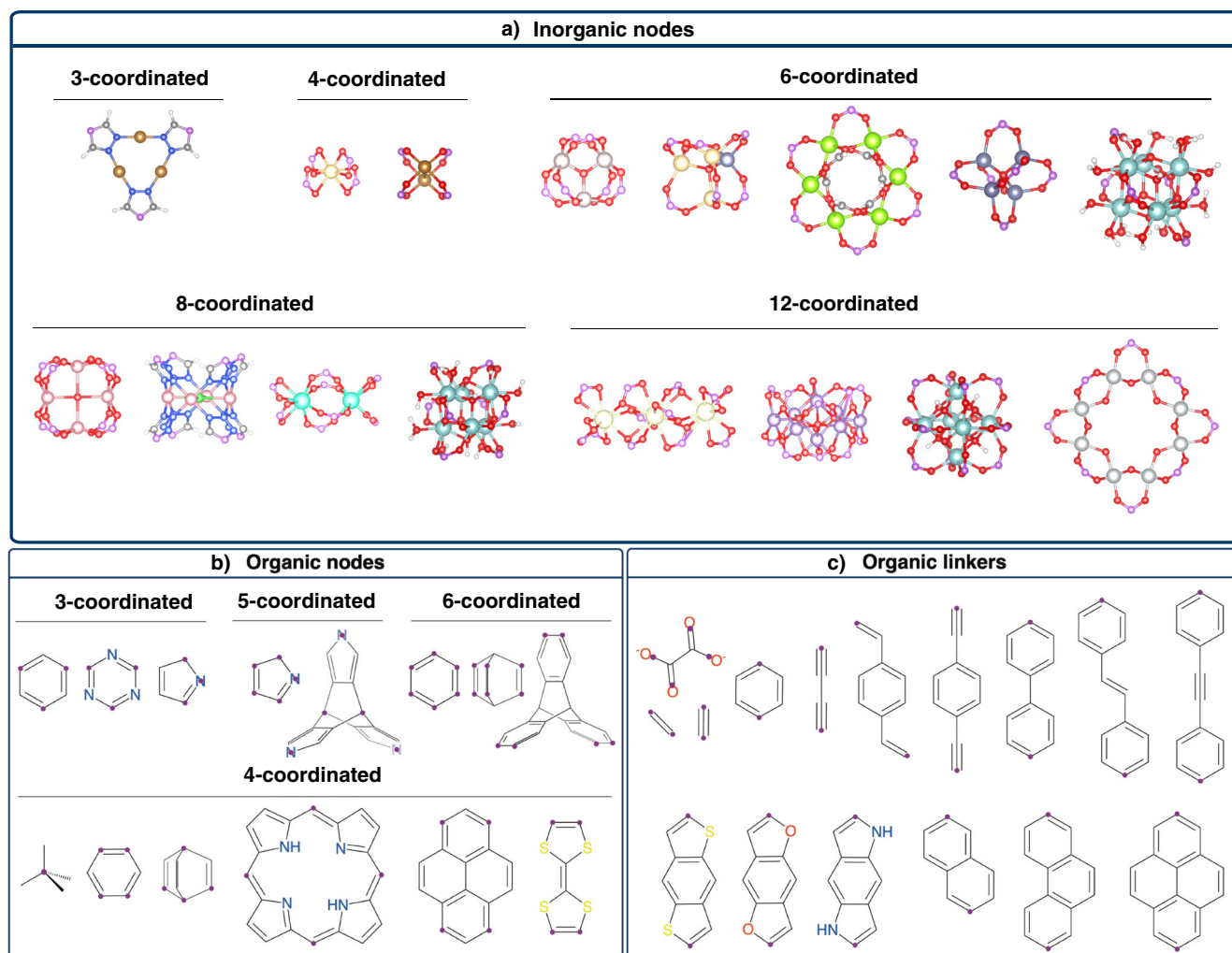


**Fig. 1** Building blocks that are used to build 10,194 hypothetical MOFs containing 1015 topologies. **a** inorganic nodes; **b** organic nodes; **c** organic linkers. The connecting points to other building blocks are represented with violet circles. For remaining inorganic nodes and organic linkers with functional groups, see Supplementary Figs. 1 and 2.

Somewhat in contrast, Cheng and coworkers studied eighteen MOFs belonging to the zeolitic imidazolate framework (ZIF) class and reported no clear correlation between MOF structural properties (e.g., pore size) and the thermal conductivity<sup>48</sup>. Instead, they found that the alignment tensor and pathway factor correlated better with thermal conductivity<sup>48</sup>. Ying and coworkers computationally studied the effect of functional group substitutions (-H, -CH<sub>3</sub>, -Br, -Cl) on the thermal conductivity of ZIF-8<sup>42</sup>. They found that ZIF-8(-CH<sub>3</sub>) showed the highest thermal conductivity, followed by ZIF-8(-H), ZIF-8(-Br), and ZIF-8(-Cl). A recent study by Wieser et al. found the node-linker bond to be the most significant bottleneck for heat transport in MOFs<sup>43</sup>. These authors reported that decreasing the mass mismatch between the metal node and organic linker in MOF-5 and MOF-508, combined with enhancing the node-linker bond strength, would increase thermal conductivity.

While the above-mentioned studies demonstrate important progress in our understanding of thermal transport in porous materials, all of them nevertheless focus on only a small number of materials. Hence, it is difficult to know whether their conclusions generalize broadly across wider ranges of MOFs, or other porous materials. A more systematic, data-driven approach where much larger numbers of MOFs are sampled could potentially cement or correct previously hinted structure-property relationships, as well as reveal previously hidden relationships.

To this end, here we report large-scale computational screening study of thermal transport characteristics in MOFs. We used classical molecular dynamics (MD) simulations to calculate the thermal conductivities of 10,194 hypothetical MOFs created using the Topology-Based Crystal Constructor (ToBaCCo) code (version 3.0)<sup>50</sup>. These 10,194 MOFs span 1,015 different topologies and include 40 types of organic edge building blocks, along with 38 inorganic and organic nodular building blocks. The building blocks are illustrated in Fig. 1 and Supplementary Figs. 1 and 2. In addition to the unveiling of structure-property relationships, we identified several MOFs with exceptionally low and high thermal conductivities and discuss their structures in more detail.

As is common when exploring hypothetical MOF structures, the synthesizability of any particular generated structure is not guaranteed. In a recent study<sup>51</sup> some of us illustrated that the calculation of free energies in hypothesized MOF structures can shed some light into their synthesizability. For instance, we found that experimentally reported MOFs among 8000+ generated MOF structures all presented free energies (at 300 K) below ~46 meV per atom. Nevertheless, generating hypothetical MOFs that are guaranteed to be physically realizable is still an unsolved challenge. In this study, our goal was to identify broad structure-property relationships and to unveil structural features and chemical motifs that may imbue MOFs with desired thermal conductivities.

## RESULTS AND DISCUSSION

Consistent with the known propensity of MOFs to present low thermal conductivity  $k$ , about 97% of the studied MOFs presented calculated average thermal conductivity values lower than  $1 \text{ W m}^{-1} \text{ K}^{-1}$  at 300 K (Fig. 2). Thus, we generally discuss structure-property relationships relating to thermal conductivities

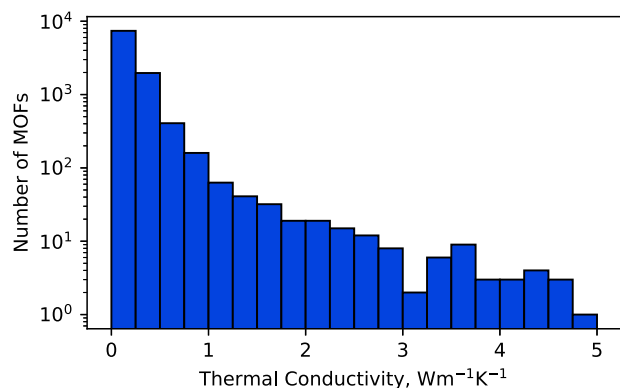


**Fig. 2 The distribution of thermal conductivity data.** The distribution of the average thermal conductivity values ( $< 5 \text{ W m}^{-1} \text{ K}^{-1}$ ) of hypothetical MOFs (bin size =  $0.25 \text{ W m}^{-1} \text{ K}^{-1}$ ). The vertical axis is logarithmic.

in the range of  $0\text{--}1 \text{ W m}^{-1} \text{ K}^{-1}$ , except when we specifically discuss the smaller number of MOFs that presented high-thermal conductivity in the *High-Thermal Conductivity MOFs* section. Here, the average thermal conductivity is the average of the  $x$ -,  $y$ -, and  $z$ -directional thermal conductivity values. To study the structure-thermal conductivity relationships governing MOFs in the range of  $0\text{--}1 \text{ W m}^{-1} \text{ K}^{-1}$ , we only considered the average thermal conductivity of each structure. The anisotropic thermal conductivity is discussed for MOFs exhibiting high thermal conductivity ( $> 10 \text{ W m}^{-1} \text{ K}^{-1}$ ). In this study we do not look into the influence of adsorbates on the thermal conductivity, which was reported and discussed elsewhere<sup>36,40,41</sup>. Thus, all calculated thermal conductivity values are for empty hypothetical MOF structures.

### Relationships between pore structure and $k$

In alignment with previous studies, thermal conductivity generally increases with MOF density (Fig. 3)<sup>48,49,52</sup>. Specifically, almost all structures with  $k > 0.2 \text{ W m}^{-1} \text{ K}^{-1}$  have a density  $> 0.2 \text{ g cm}^{-3}$ , whereas structures with comparatively higher  $k$  ( $> 0.5 \text{ W m}^{-1} \text{ K}^{-1}$ ) have a density  $> 0.5 \text{ g cm}^{-3}$ . In contrast, for low  $k$  MOFs ( $< 0.1 \text{ W m}^{-1} \text{ K}^{-1}$ ), a wide spread of densities ( $0\text{--}2 \text{ g cm}^{-3}$ ) can be observed. Figure 3 also shows that even though the density is correlated with  $k$ , density alone is not sufficient in accounting for differences in  $k$ . For example, at a density of  $1 \text{ g cm}^{-3}$ , a wide span of  $k$  values, ranging from  $0.05 \text{ W m}^{-1} \text{ K}^{-1}$  to  $0.75 \text{ W m}^{-1} \text{ K}^{-1}$ , can

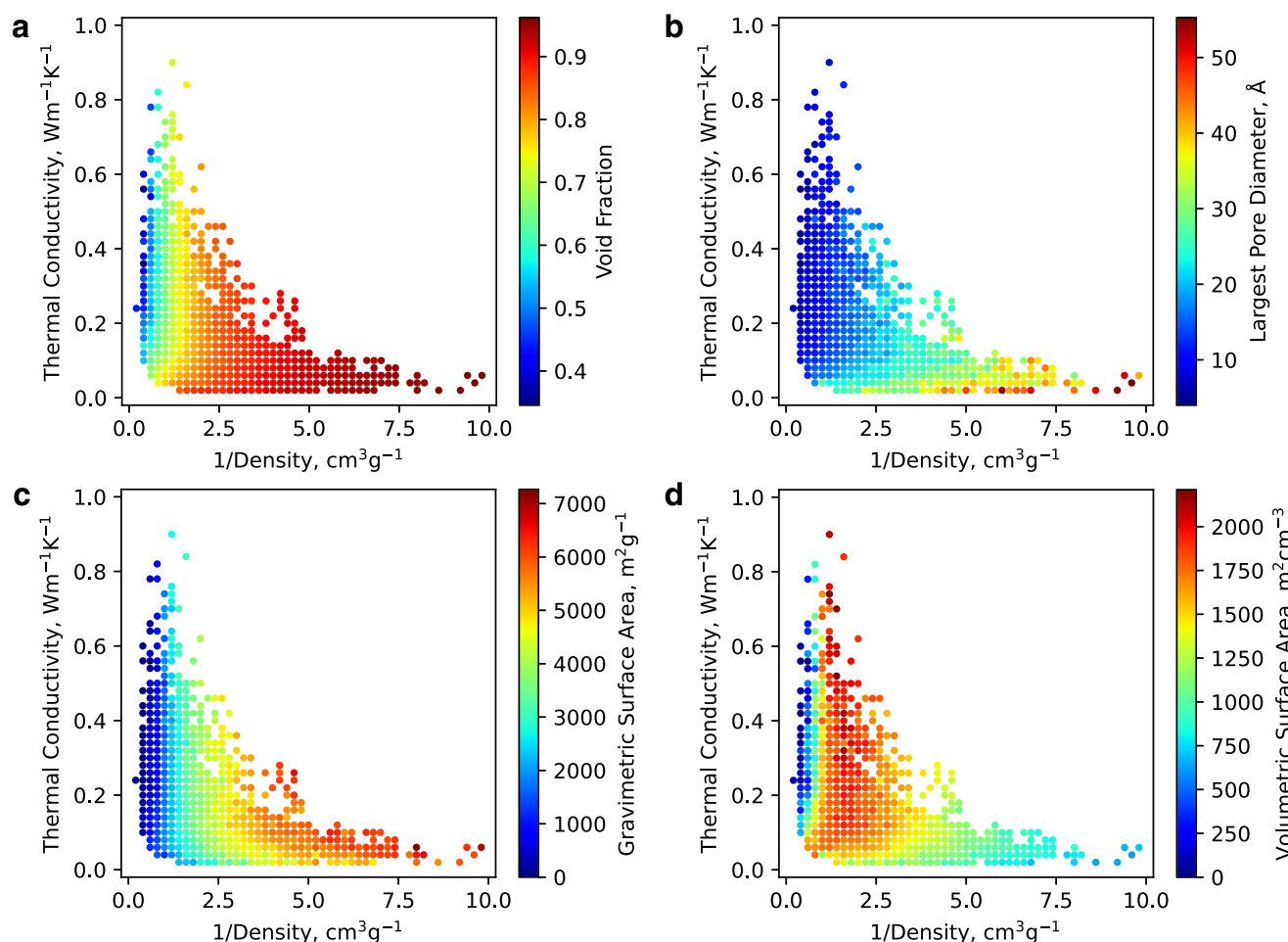


**Fig. 3 Relationships between average thermal conductivity and inverse density.** Figure panels are colored by **a** void fraction, **b** largest pore diameter, **c** gravimetric surface area, and **d** volumetric surface area. Each plot is divided into  $50 \times 50$  bins which are illustrated by a filled circle, whose color represents the averaged property across all MOFs in that bin. Bins with less than three structures are not shown to reduce noise.

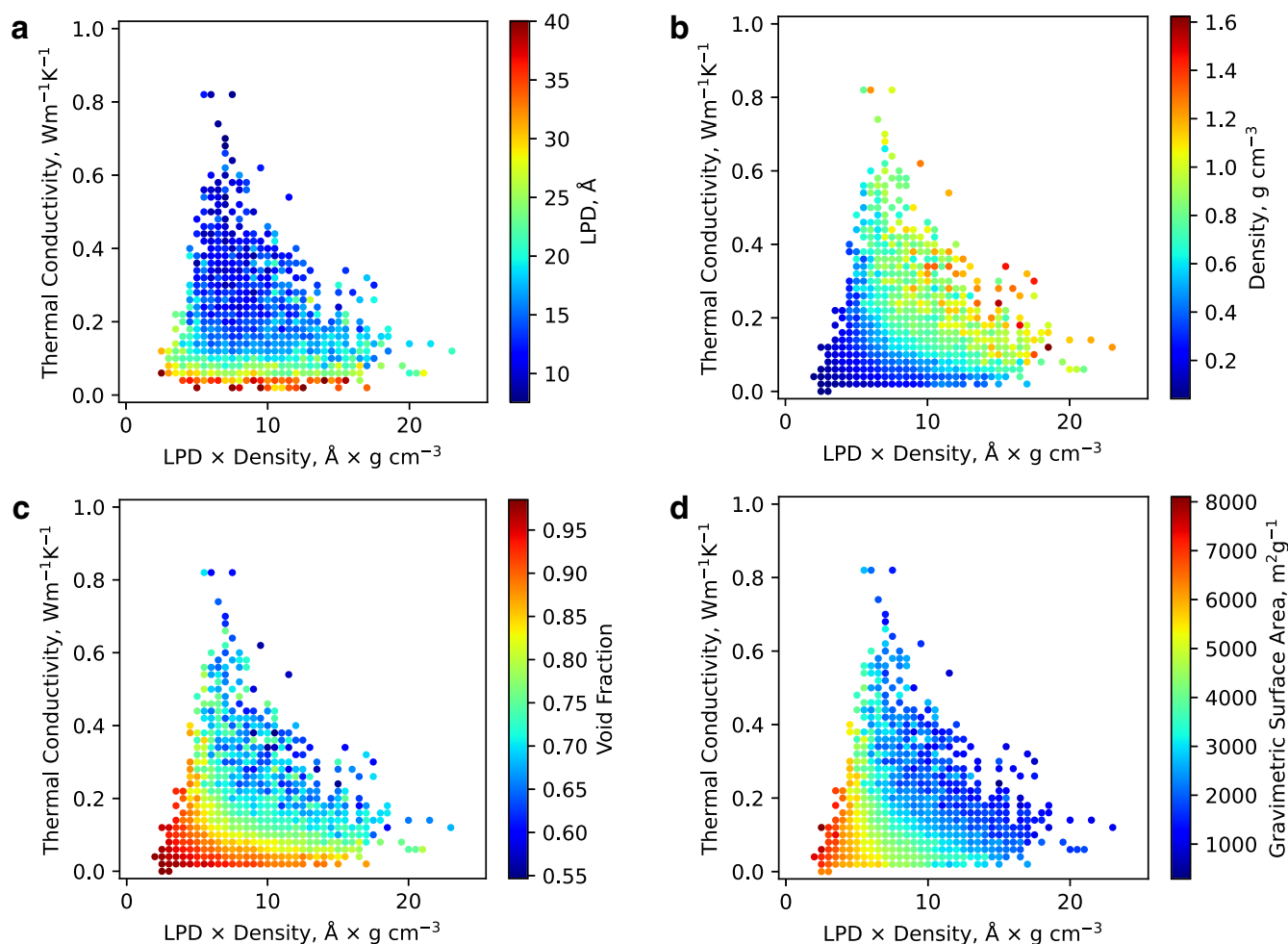


**Fig. 4** Relationship between thermal conductivity and the product of the density and the largest pore diameter (LPD). Figure panels are colored by **a** LPD, **b** density, **c** void fraction, and **d** gravimetric surface area. Each plot is divided into  $50 \times 50$  bins which are illustrated by a filled circle, whose color represents the averaged property across all MOFs in that bin. Bins with less than three structures are not shown to reduce noise.

be found. This result adds nuance to prior findings, which reported a linear correlation between  $k$  and MOF density but considered significantly fewer materials<sup>48,52</sup>. Such insights highlight the advantages of a large and diverse MOF data set for observing structure-property relationships.

As shown in Fig. 3a, all structures with high  $k > 0.6 \text{ W m}^{-1} \text{ K}^{-1}$  have void fractions less than 0.9, whereas all structures with extremely low  $k < 0.04 \text{ W m}^{-1} \text{ K}^{-1}$  have void fractions greater than 0.8. Given the high correlation of density and void fraction, it is unsurprising that a lower void fraction results in a higher  $k$ . Cheng and coworkers also reported a negative correlation between  $k$  and the void fraction (Pearson correlation coefficient =  $-0.82$ ) for eighteen ZIFs with unique topologies<sup>48</sup>. An intermediate  $k$  value ( $0.1\text{--}0.6 \text{ W m}^{-1} \text{ K}^{-1}$ ) can have all possible values of void fraction considered ( $0.35\text{--}0.95$ ). According to Fig. 3b, as the pore size increases, the thermal conductivity decreases, which agrees well with the results from previous studies<sup>37,48,49,52</sup>. All structures with  $k > 0.5 \text{ W m}^{-1} \text{ K}^{-1}$  have a largest pore diameter (LPD) of  $< 25 \text{ \AA}$ . The relationship between  $k$  and pore limiting diameter (PLD) can be found in Supplementary Fig. 10, which is very similar to that between  $k$  and LPD. Figure 3c illustrates that for  $k < 0.2 \text{ W m}^{-1} \text{ K}^{-1}$ , at any density within the range of  $0.25\text{--}0.5 \text{ g cm}^{-3}$  (or  $2\text{--}4 \text{ cm}^3 \text{ g}^{-1}$  of  $1/\text{density}$ ), the value of  $k$  increases as the gravimetric surface area (GSA) increases due to a decrease in LPD. For instance, at a density value of  $0.3 \text{ g cm}^{-3}$ , when the GSA increases from

$\sim 3000 \text{ m}^2 \text{ g}^{-1}$  to  $5000 \text{ m}^2 \text{ g}^{-1}$ ,  $k$  soars from a very low value of about  $0.03 \text{ W m}^{-1} \text{ K}^{-1}$  to an intermediate value of  $0.15 \text{ W m}^{-1} \text{ K}^{-1}$ , which is a five-fold increase.

A similar trend can be observed in Fig. 3d:  $k$  can be improved by increasing the volumetric surface area (VSA) at densities in the  $\sim 0.25\text{--}0.5 \text{ g cm}^{-3}$  range. Interestingly, structures with the same VSA can have different densities, and thus different  $k$  values. For example, in Fig. 3d, the data shows that at  $1/\text{density}$  values of around  $1 \text{ cm}^3 \text{ g}^{-1}$  and  $6 \text{ cm}^3 \text{ g}^{-1}$  one can have high ( $> 0.8 \text{ W m}^{-1} \text{ K}^{-1}$ ) or very low ( $< 0.05 \text{ W m}^{-1} \text{ K}^{-1}$ ) values of  $k$  while maintaining the same VSA. This finding could be important for gas adsorption applications, where the VSA strongly influences the amount of gas adsorbed but a high  $k$  is desired for the target application.

Typically, high and low densities correspond to small and large pore sizes, respectively. It is uncommon for a material to have a high density and large pore sizes simultaneously. Thus, to find the optimal combination of properties, we considered thermal conductivity as a function of the product of pore size and density (see Fig. 4).

As shown in Fig. 4, thermal conductivity sharply decreases when  $\text{LPD} \times \text{density}$  is too small or too large. We found an optimal  $\text{LPD} \times \text{density}$  region in the  $5\text{--}10 \text{ \AA g cm}^{-3}$  range, which corresponds to an  $\text{LPD} < 15 \text{ \AA}$  and a density range of  $\sim 0.8\text{--}1.4 \text{ g cm}^{-3}$ . However, an optimal  $\text{LPD} \times \text{density}$  range alone is not enough to ensure

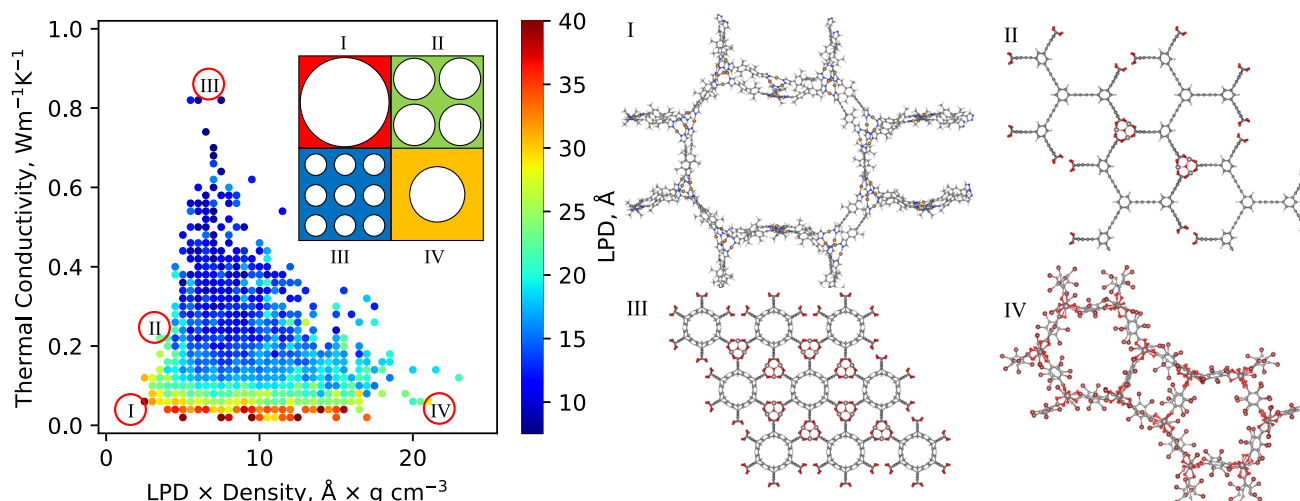


**Fig. 5** Images of hypothetical MOF structures from different regions of the structure-thermal conductivity space. The figure on the left illustrates where each structure is located with respect to the product of the density and the largest pore diameter (LPD): (I) very low density and very high LPD, (II) low density and high LPD, (III) high density and low LPD, (IV) high density and high LPD. The inset figure illustrates how structures in each region look qualitatively with respect to the relative pore size and density. The pore diameter is adjusted proportionally to the average pore diameter in each region.

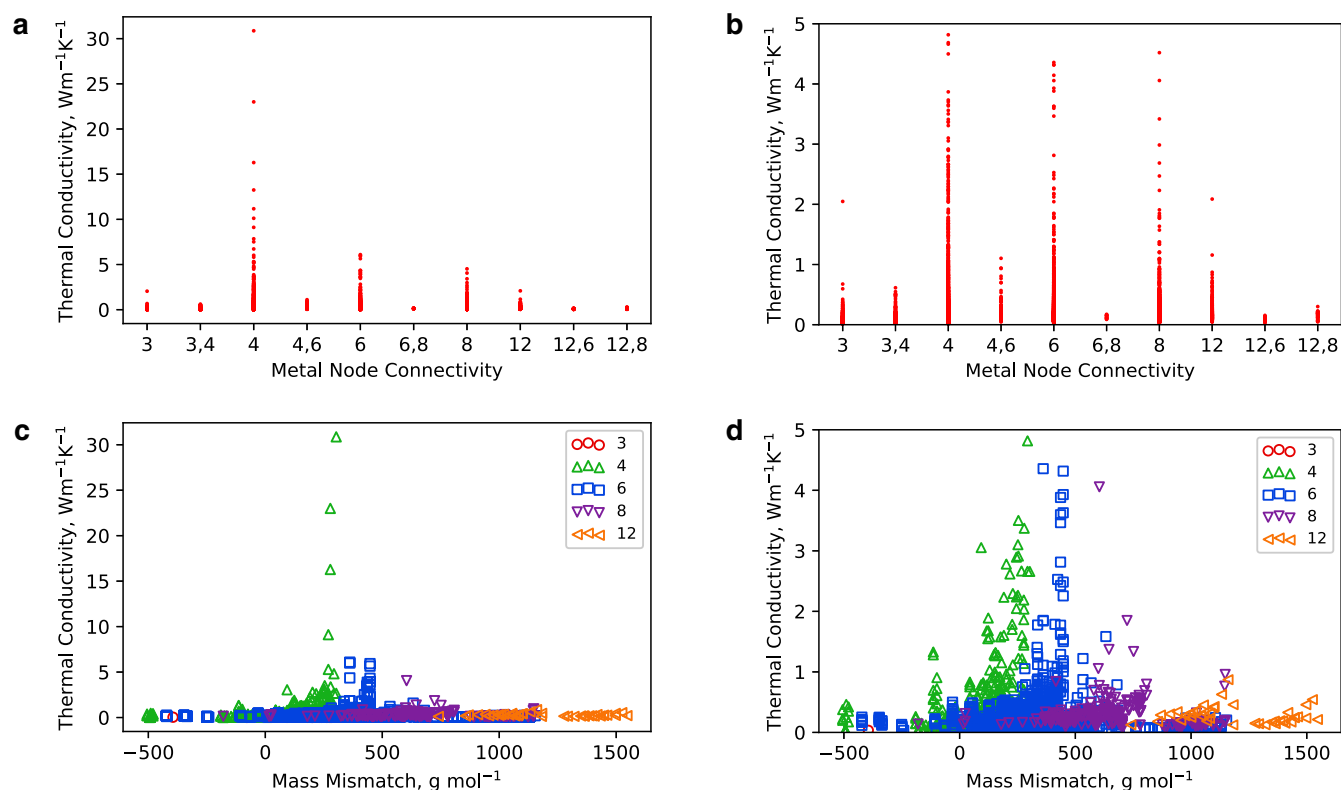
high conductivity; for example, within an LPD  $\times$  density range of 5–10  $\text{\AA} \text{ g cm}^{-3}$ , MOFs with very low  $k$  can be found (i.e., those with LPD's  $> 30 \text{\AA}$  and densities  $< 0.4 \text{ g cm}^{-3}$ , as seen in Fig. 4a, b). Perhaps not surprisingly, a high LPD alone is sufficient to achieve a low  $k$ . However, other structural properties such as density, void fraction, and GSA alone do not guarantee a low conductivity (Fig. 4b, c, d). Thus, for MOF structures to achieve a low  $k$ , only the LPD must be high, but many properties must align to achieve a high  $k$ . At a constant density of  $\sim 0.6 \text{ g cm}^{-3}$ , if you move to the left along the light blue circles in Fig. 4b, the thermal conductivity increases, which correlates with a decrease in pore size. A similar trend can also be observed for the void fraction and gravimetric surface area (Fig. 4c, d). For instance,  $k$  increases in moving to the left along yellow or green circles at a void fraction range of 0.75–0.85. To sum up, a high  $k$  favors high density, small pores, an intermediate value of void fraction (0.6–0.7), and a small GSA (2000–3000  $\text{m}^2 \text{ g}^{-1}$ ).

Figure 5 illustrates hypothetical MOF structures from different regions of the MOF structure-property space. In region I, where MOFs have a very low density ( $\sim 0.06 \text{ g cm}^{-3}$ ) and huge pores ( $\sim 50 \text{\AA}$ ),  $k$  is very low ( $\sim 0.04 \text{ W m}^{-1} \text{ K}^{-1}$ ). Such low  $k$  values can be ascribed to a low areal concentration of bonded interactions<sup>37</sup>. In region II,  $k$  is improved by nearly an order of magnitude ( $\sim 0.24 \text{ W m}^{-1} \text{ K}^{-1}$ ) compared to region I since the density increased to  $\sim 0.2 \text{ g cm}^{-3}$  and the LPD became smaller ( $\sim 24 \text{\AA}$ ). Region III shows the highest  $k$  value ( $\sim 0.85 \text{ W m}^{-1} \text{ K}^{-1}$ ), which corresponds to a high density ( $\sim 0.82 \text{ g cm}^{-3}$ ) and a low LPD ( $\sim 10 \text{\AA}$ ). This is an optimal region for high  $k$  since it possesses the highest areal density of bonded interactions. Finally, in region IV, as LPD increases ( $\sim 32 \text{\AA}$ ) at a density close to region III, the  $k$  drops again to a very low value ( $\sim 0.06 \text{ W m}^{-1} \text{ K}^{-1}$ ). Although regions III and IV have a similar density, region IV has  $\sim 3$  times larger pore diameters but  $\sim 14$  times lower  $k$  than region III. This additionally supports our observation that pore size has a more pronounced impact on  $k$  than density. Moreover, region IV has an LPD  $\sim 1.56$  times lower than region I, but  $\sim 13$  times higher density. In these MOFs, a higher density is typically due to heavier building blocks (e.g., high-coordinated nodes and functionalized linkers) for a material with similar pore sizes. This result implies that for MOFs with very large pore sizes (e.g.,  $> 30 \text{\AA}$ ), increasing the density by using heavier building blocks might not appreciably impact  $k$ .

For most applications of MOFs, the adsorption capacity is still the primary consideration even if  $k$  is also an important property. Thus, it is helpful to consider the surface area available for adsorption in each of these regions. Regarding void fraction and GSA, region I has an ultra-high void fraction ( $\sim 0.97$ ) and GSA ( $\sim 7200 \text{ m}^2 \text{ g}^{-1}$ ) due to huge voids and low density. Region II has higher  $k$  than region I and a slightly lower void fraction ( $\sim 0.92$ ) and GSA ( $\sim 6700 \text{ m}^2 \text{ g}^{-1}$ ). From region II to III, the void fraction decreases from 0.92 to 0.69, whereas GSA drop significantly from 6700  $\text{m}^2 \text{ g}^{-1}$  to 2400  $\text{m}^2 \text{ g}^{-1}$  due to increased density. Region IV has the lowest GSA of 1600  $\text{m}^2 \text{ g}^{-1}$  with a comparable  $k$  as region I, where GSA is the largest ( $\sim 7200 \text{ m}^2 \text{ g}^{-1}$ ). We note that the optimal region that gives rise to high  $k$  ( $> 0.8 \text{ W m}^{-1} \text{ K}^{-1}$ ) might not possess optimal gas adsorption capacity due to having a low GSA. Balancing volumetric and gravimetric uptake is important in gas storage applications<sup>53</sup>. Thus, to determine the optimal combination of  $k$  and deliverable capacity, we plotted  $k$  versus LPD  $\times$  density with the data points colored by VSA  $\times$  GSA (see Supplementary Fig. 11). We found the ideal VSA and GSA trade-off corresponds to an LPD  $\times$  density of  $\sim 5 \text{\AA} \text{ g cm}^{-3}$  with an LPD of  $< 20 \text{\AA}$ . This condition corresponds to an average void fraction of 0.85, which is also the ideal void fraction for methane and hydrogen storage reported by Chen et al.<sup>53</sup>. As shown in Supplementary Fig. 11, the highest average  $k$  for ideal VSA  $\times$  GSA is capped at  $\sim 0.5 \text{ W m}^{-1} \text{ K}^{-1}$ , whereas the lower bound can go down to  $\sim 0.1 \text{ W m}^{-1} \text{ K}^{-1}$ . Here, we at least show that thermal transport in MOFs can be optimized simultaneously in conjunction with other specific target properties.

#### Relationships between compositional/geometric characteristics and $k$

In addition to structural characteristics (pore size, surface area, void fraction, etc.), we investigated the influence of two compositional/geometric properties of MOFs on the thermal conductivity: metal node connectivity (coordination number) and mass mismatch between the node and the organic linker. We did not consider the bonding chemistry (e.g., bond strength) between the metal node and the linker, which was investigated elsewhere, albeit not comprehensively<sup>43</sup>. Some MOF structures contain two types of metal node connectivity, as shown in Fig. 6a, b.



**Fig. 6 Thermal conductivity and compositional/geometric characteristics.** Relationships of the average thermal conductivity with metal node connectivity (a, b) and node-linker mass mismatch (c, d). The figures (a, b) and (c, d) are the same plots but with a different vertical scale. In figures (a, b), the pairs of numbers (e.g., 3,4 and 12,6) mean two different types of metal node connectivity in a structure. Colors: red (3-connected), green (4-connected), blue (6-connected), purple (8-connected), and orange (12-connected).

Notably, we find that all MOFs with exceptionally high  $k$  ( $> 10 \text{ W m}^{-1} \text{ K}^{-1}$ ) have a metal node connectivity of 4, which is intriguing, since diamond, the best-known heat conductor ( $2200 \text{ W m}^{-1} \text{ K}^{-1}$  at  $300 \text{ K}$ )<sup>54</sup>, and cubic boron arsenide ( $1300 \text{ W m}^{-1} \text{ K}^{-1}$  at  $300 \text{ K}$ )<sup>55</sup>, also have 4-connected crystal network topologies. This suggests that topology could be an important factor in designing high- $k$  MOFs. Moreover, several structures with 6 and 8 coordination also show relatively large values of  $k$  ( $> 5 \text{ W m}^{-1} \text{ K}^{-1}$ ). Structures with low-coordinated (3) and high-coordinated (12) nodes exhibit lower  $k$  values ( $< 2 \text{ W m}^{-1} \text{ K}^{-1}$ ), with the majority being even lower than  $1 \text{ W m}^{-1} \text{ K}^{-1}$ , which is typical of MOFs. Likewise, all of the evaluated MOFs with two different types of metal node connectivity show lower  $k$ , with 4,6 coordination possessing the highest  $k$  among these ( $1.1 \text{ W m}^{-1} \text{ K}^{-1}$ ), followed by 3,4 ( $0.61 \text{ W m}^{-1} \text{ K}^{-1}$ ), 12,8 ( $0.3 \text{ W m}^{-1} \text{ K}^{-1}$ ), 6,8 ( $0.17 \text{ W m}^{-1} \text{ K}^{-1}$ ), and 12,6 ( $0.15 \text{ W m}^{-1} \text{ K}^{-1}$ ).

To investigate the influence of mass mismatch between metal nodes and organic linkers on thermal conductivity, only MOFs containing a single type of linker and node (2737 MOFs) were considered. Here, a mass mismatch is defined as the difference in mass between a single node and a single linker. A positive mismatch means the node is heavier, while a negative mismatch means the linker is heavier. The relationship between  $k$  and the mass mismatch has a mountain shape (see Fig. 6c, d), with a peak in the range of  $250\text{--}500 \text{ g mol}^{-1}$  where all the highly conductive MOFs ( $k > 5 \text{ W m}^{-1} \text{ K}^{-1}$ ) are found. Similar observations were reported by Han et al.<sup>49</sup> and Wieser et al.<sup>43</sup>, where they found that reducing the mass mismatch substantially increases  $k$  in MOF-5. This was attributed to an increased overlap in the phonon density of states, minimizing phonon scattering at the node-linker interfaces. However, having a small node-linker mass difference

alone does not ensure a high conductivity, as we observe many poorly conductive MOFs also within that range.

As the positive mass difference increases (beyond  $500 \text{ g mol}^{-1}$ ),  $k$  tends to be lower ( $< 2 \text{ W m}^{-1} \text{ K}^{-1}$ ). Those regions are mainly occupied by structures with node connections of 4, 8, or 12 and greater node masses. In these structures, the node is much heavier than its linker, leading to a greater mass mismatch. Beyond  $1250 \text{ g mol}^{-1}$ , only 12-connected MOFs are encountered, for which the thermal conductivity values are below  $1 \text{ W m}^{-1} \text{ K}^{-1}$ . Conversely, for almost all structures with the negative mass mismatch, the  $k$  values are below  $1 \text{ W m}^{-1} \text{ K}^{-1}$ . The negative mass difference of greatest magnitude is about  $-500 \text{ g mol}^{-1}$ , whereas the maximum positive value exceeds  $1500 \text{ g mol}^{-1}$ . Importantly, all structures within the range of  $250\text{--}500 \text{ g mol}^{-1}$  are ones with relatively small node mass and linker mass as well. Since we are missing structures in our database with both a heavy node and a heavy linker such that the mass difference would still be relatively low, it is hard to say anything about their thermal conductivity. We also show the relationship of  $k$  with the node mass and the linker mass separately in Supplementary Figs. 13 and 14. For both the node and the linker,  $k$  increases as the mass of the corresponding building blocks decreases, indicating that the mass of the individual building blocks might also influence  $k$  in addition to the mass mismatch. For instance, all MOFs with  $k > 3 \text{ W m}^{-1} \text{ K}^{-1}$  have a node mass  $< 600 \text{ g mol}^{-1}$  and a linker mass  $< 200 \text{ g mol}^{-1}$ . Thus, a good strategy for designing highly thermally conductive MOFs, in addition to minimizing the mass mismatch, would be to choose lighter building blocks (nodes and linkers) if possible.

#### Low-thermal conductivity MOFs

Dense crystalline solids with very low thermal conductivity ( $< 0.1 \text{ W m}^{-1} \text{ K}^{-1}$ ) have attracted interest for applications such

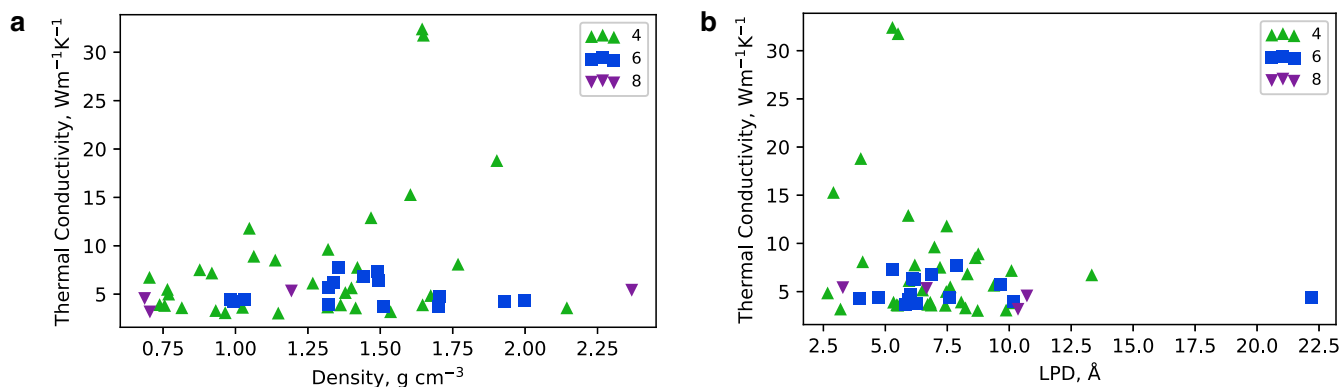


**Fig. 7** Relationships of the average thermal conductivity of the top 53 high- $k$  MOFs with density and LPD colored by metal node connectivity. **a** thermal conductivity and density; **b** thermal conductivity and largest pore diameter (LPD). Colors: green (4-connected), blue (6-connected), and purple (8-connected).

as thermal insulation and thermoelectrics<sup>56</sup>. We found that 2683 MOFs have  $k < 0.1 \text{ W m}^{-1} \text{ K}^{-1}$ , comparable to or perhaps lower than the  $k$  values typically found for polymers ( $\sim 0.1 \text{ W m}^{-1} \text{ K}^{-1}$ )<sup>56</sup>. Among them, 608 of our MOFs have  $k < 0.05 \text{ W m}^{-1} \text{ K}^{-1}$ , and 36 have  $k < 0.02 \text{ W m}^{-1} \text{ K}^{-1}$ . To compare, the lowest reported experimental thermal conductivity at room temperature of any known dense solids was  $0.03 \text{ W m}^{-1} \text{ K}^{-1}$  in fullerene derivative PCBM<sup>57</sup>. The average LPD of all MOFs with  $k < 0.1 \text{ W m}^{-1} \text{ K}^{-1}$  is  $\sim 30 \text{ \AA}$ , whereas it is  $\sim 42 \text{ \AA}$  and  $\sim 65 \text{ \AA}$  for MOFs with  $k < 0.05 \text{ W m}^{-1} \text{ K}^{-1}$  and  $k < 0.02 \text{ W m}^{-1} \text{ K}^{-1}$ , respectively, which again shows the significant impact of pore size on  $k$ . The average void fractions for all MOFs with  $k < 0.1 \text{ W m}^{-1} \text{ K}^{-1}$  and  $k < 0.02 \text{ W m}^{-1} \text{ K}^{-1}$  are  $\sim 0.88$  and  $\sim 0.96$ , respectively. This result again shows that high porosity and large pores are primarily responsible for ultra-low thermal conductivity in MOFs, which could be ascribed to an extraordinarily low density of bonded interactions. Although MOFs usually exhibit low  $k$ , we note that it could be further reduced by creating even larger voids (e.g., via defect engineering, hierarchical pore structures) for emerging applications such as thermoelectric materials that necessitate thermal insulation<sup>21–25</sup>. However, we note that it is extremely challenging to activate a MOF with exceptionally large pores without having the structure collapse upon solvent removal<sup>58</sup>. Unlike MOFs, other non-porous dense solids might require different means of reducing  $k$ , such as a systematic layering of materials<sup>59</sup>.

### High-thermal conductivity MOFs

A small subset of 105 MOFs in our screening showed thermal conductivity higher than  $2 \text{ W m}^{-1} \text{ K}^{-1}$ . To investigate these structures further, we repeated our thermal conductivity calculations using a higher number of timesteps (1 ns) and greater correlation lengths (100 ps) for increased accuracy. Among the higher quality simulation predictions, 53 MOFs were found to have  $k > 3 \text{ W m}^{-1} \text{ K}^{-1}$ , of which 28 had  $k > 5 \text{ W m}^{-1} \text{ K}^{-1}$  and 6 had  $k > 10 \text{ W m}^{-1} \text{ K}^{-1}$ . Surprisingly, we found two MOFs with values of  $k$  over  $30 \text{ W m}^{-1} \text{ K}^{-1}$ , which is comparable in thermal conductivity to a semiconductor such as GaAs ( $55 \text{ W m}^{-1} \text{ K}^{-1}$ )<sup>60</sup>. More than 70% of these structures have a density  $> 1 \text{ g cm}^{-3}$ , and almost all of them ( $\sim 90\%$ ) have small pores ( $< 10 \text{ \AA}$ ), as illustrated in Fig. 7a, b. The average density and LPD of all 53 high- $k$  MOFs are  $1.3 \text{ g cm}^{-3}$  and  $7.2 \text{ \AA}$ , respectively.

As mentioned earlier, we found a surprisingly strong connection between high thermal conductivity and MOFs with crystal network topologies possessing 4-connected nodes. About 65% of the top 53 MOFs have 4-connected nodes, whereas all of the top ten MOFs with the highest  $k$  values ( $> 8 \text{ W m}^{-1} \text{ K}^{-1}$ ) have exclusively 4-connected nodes. Recently, a computational study of

covalent-organic frameworks (COFs) showed that a COF-300 derivative with a small pore size ( $\sim 6.3 \text{ \AA}$ ) could exhibit ultra-high thermal conductivity ( $> 15 \text{ W m}^{-1} \text{ K}^{-1}$ ), which is unusual for a 3D polymer<sup>61</sup>. Interestingly, this COF-300 derivative also has a 4-connected topology. Additionally, Giri et al. reported that changing the concentration of the  $\text{sp}^3$ -bonded carbon atoms (four-fold coordination) from  $\sim 10\%$  to  $\sim 80\%$  results in an increase of the thermal conductivity by four-fold in amorphous carbon<sup>62</sup>. This was attributed to an increased contribution from the propagating vibrational modes (propagons) at higher  $\text{sp}^3$  content, revealing the significance of the influence of atomic coordination on the fundamental vibrational characteristics of materials. We think that this 4-connected node observation is significant to achieving very high thermal conductivity in MOFs, although a precise mechanistic understanding of why this topology (and not others) leads to high  $k$  remains an open question.

All six highly conductive MOFs with average  $k > 10 \text{ W m}^{-1} \text{ K}^{-1}$  have perpendicular 4-connected square planar metal nodes (e.g., Cu(II)-paddlewheel), where five of them have a perpendicular node-linker connection that forms a cage-like structure with rectangular shaped pores (see Table 1 and Supplementary Figs. 16–19). In Fig. 8, we show one of the two ultra-high  $k$  MOFs (cdz topology), which had an average thermal conductivity of  $31.8 \text{ W m}^{-1} \text{ K}^{-1}$ . It is important to stress that in large-scale screening studies such as this one, structure-property relationships across many materials are more reliable than insights from any individual structure. Nevertheless, with appropriate caution, we think useful insights may be hypothesized from considering the singular MOF with the highest thermal conductivity in our dataset in more detail, even if that MOF may not be synthesizable or its features not well represented among the majority of the hypothetical MOFs considered. Particularly, we note that the oxalate linkers in this MOF would likely prefer to chelate  $\text{Cu}^{2+}$  in a way that forms five-membered rings instead of the four-connected paddlewheel structure assumed in the hypothetical MOF generation code.

This ultra-high  $k$  MOF consists of a square planar Cu(II)-paddlewheel as a metal node and oxalate (planar and twisted) as an organic linker. The twisted oxalate linkers run along the  $y$ -direction, but they all are planar in the  $x$ - and  $z$ -directions. It exhibits a very high anisotropy, showing ultra-high thermal conductivity in two directions and relatively low thermal conductivity in the other ( $24.8 \text{ W m}^{-1} \text{ K}^{-1}$ ,  $2.5 \text{ W m}^{-1} \text{ K}^{-1}$  and  $68.1 \text{ W m}^{-1} \text{ K}^{-1}$  in  $x$ -,  $y$ -, and  $z$ -directions, respectively). We hypothesize that an important feature of this MOF is that its nodes connected along the highest- $k$  direction have minimal perpendicular connections. High thermal conductivity in the  $x$ -direction ( $24.8 \text{ W m}^{-1} \text{ K}^{-1}$ ) is mainly contributed to by strong covalent bonds along the  $x$ -direction in the  $xz$  plane (planes



Formula	Topology	Density ( $\text{g cm}^{-3}$ )	LPD ( $\text{\AA}$ )	VF	$k$ ( $\text{W m}^{-1} \text{K}^{-1}$ )	Node	Organic linker
$\text{V}(\text{C}_2\text{O}_4)$	cdm	1.64	5.29	0.52	32.4		
$\text{Cu}(\text{C}_2\text{O}_4)$	cdz	1.65	5.51	0.57	31.8		
$\text{V}(\text{C}_2\text{O}_4)$	qdl	1.90	4.01	0.45	18.8		
$\text{Cu}(\text{C}_{10}\text{O}_4)$	nor	1.60	2.90	0.44	15.3		
$\text{V}_2(\text{C}_5\text{HO}_8)$	cdn	1.47	5.92	0.56	12.9		
$\text{V}_3(\text{C}_9\text{HO}_{12})$	cdz	1.05	7.48	0.67	11.8		

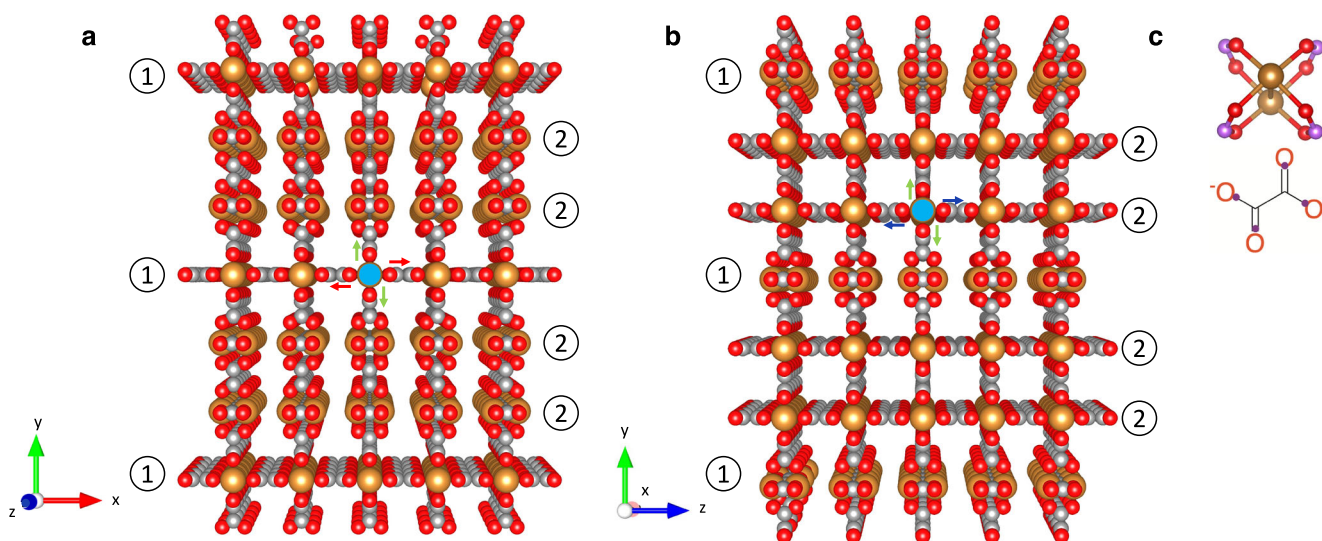


**Fig. 8** Cross-sectional views of the ultra-high thermal conductivity MOF structure (cdz topology). The color scheme for the atoms is as follows: copper (gold), oxygen (red), carbon (dark grey); Panel (b) is (a) rotated clockwise by 90 degrees around the  $y$ -axis. The circled 1 and 2 represents the  $xz$  planes. **c** building blocks: a Cu(II)-paddlewheel metal node and an oxalate linker. The connecting points to other building blocks are represented with violet circles.

numbered 1), where the contribution by nonbonded interactions in the  $x$ -direction (planes numbered 2) is weak. In the  $z$ -direction, the thermal conductivity is the highest ( $68.1 \text{ W m}^{-1} \text{K}^{-1}$ ), which is also helped by strong covalent bonds along the  $z$ -direction on the  $xz$  plane (planes numbered 2). This is the highest directional thermal conductivity observed in this work.

Finally, the  $y$ -direction has the lowest thermal conductivity ( $2.5 \text{ W m}^{-1} \text{K}^{-1}$ ). We think this is because connections in the  $y$ -direction are not uniform direction-wise: some nodes have a connection in the  $x$ - and  $y$ -directions (blue node in Fig. 8a), but others are connected to nodes in the  $z$ - and  $y$ -directions (blue node in Fig. 8b) because of the twisted oxalate linkers. We hypothesize that having additional connections in a third dimension across the plane along the pathway of heat transport (direction  $y$  in Fig. 8a, b) disturbs the phonon vibrations along that direction, resulting in increased phonon scattering and hence, lower thermal conductivity. Note that the additional connection is

necessary, however, to form a stable 3D MOF structure by connecting the otherwise unconnected 2D sheets (e.g., the  $xy$  planes are connected via  $z$ -direction in Fig. 8a, b).

A decade ago, a single isolated polyethylene chain was predicted via simulations to have exceptionally high  $k$  in the chain direction<sup>63</sup>. Subsequently, it was experimentally measured that ultra-drawn polyethylene nanofibers can also exhibit very high  $k$  ( $104 \text{ W m}^{-1} \text{K}^{-1}$ ), the highest reported experimental  $k$  for a polymer at the time<sup>64</sup>. However, the  $k$  of ultra-drawn polyethylene nanofibers was not expected to approach the predicted  $k$  of a single isolated chain due to increased phonon-phonon scattering within each chain that resulted from chain-chain van der Waals interactions<sup>64,65</sup>. The structure shown in Fig. 8 suggests that the same design concept may be applicable to MOFs.

By analogy, we can think of the bonded atoms in this MOF in each direction as individual chains. The  $y$ -direction has the lowest  $k$  since it has many perpendicular bonded interactions, leading to

**Table 2.** A summary of the strategies for designing MOFs with low/high thermal conductivities.**For High Thermal Conductivity**

- Use high density ( $> 1.0 \text{ g cm}^{-3}$ ), small pores ( $< 10 \text{ \AA}$ ), and small void fraction ( $\sim 0.5$ )
- Use 4-connected square planar metal-based nodes to connect the organic linkers in a perpendicular orientation
- Keep the mass mismatch between the node and the linker in the range of  $250\text{--}500 \text{ g mol}^{-1}$ . Use lighter building blocks (nodes and linkers)
- The thermal conductivity can be improved in a particular direction by aligning the bonded atoms parallel to it and reducing the number of perpendicular bonded interactions. This is facilitated when 4-connected square planar nodes are used
- MOF structures can be designed to maximize thermal conductivity in the two directions by sacrificing in the third direction. Several topologies (cdm, cdz, cdm, qdl, ukk) in our database possess this feature
- Use short, linear organic linkers (e.g., oxalate, acetylenedicarboxylate)
- Topology (particularly 4-connected networks) has a significant impact on thermal conductivity

**For Low Thermal Conductivity**

- Use large pores ( $> 30 \text{ \AA}$ ) and high void fractions ( $> 0.88$ )
- Increasing only the pore size is usually sufficient to achieve a low thermal conductivity

more scattering, whereas such interactions are minimized in the other two directions. It may be that the 4-connected square-planar nodes featured in our most highly conductive MOFs help facilitate such a design strategy, where high directional thermal transport along one axis has minimal perpendicular scattering. In contrast, while 3-connected nodes give even fewer bonded-interactions perpendicular to thermal transport, it is hard to get highly aligned bonded heat transfer pathways in the parallel direction. With 6-connected (and higher connectivity) nodes, the increase in aligned heat transfer pathways is outweighed by bonded connections in perpendicular directions, as in MOF-5<sup>30</sup>. Cheng and coworkers introduced an alignment tensor to explain high thermal conductivity in MOFs that also supports our hypothesis described here<sup>48</sup>.

The thermal conductivity may vary considerably within the same topology if structural and compositional characteristics differ. Even with a suitable topology, it is possible to attain a low thermal conductivity if the right combination of structural and compositional properties is not selected. For instance, we have several structures with average  $k < 1 \text{ W m}^{-1} \text{ K}^{-1}$  but that share the same topology (cdz topology) as the MOF with the highest conductivity ( $k > 30 \text{ W m}^{-1} \text{ K}^{-1}$ ). However, the reverse is not true, as it appears that the highest thermal conductivity structures are confined to a narrow subset of possible topologies. No matter what structural or compositional characteristics a MOF contains, it is impossible to achieve an outstanding thermal conductivity if the wrong topology is adopted. For instance, some topologies in our database never showed a high thermal conductivity even if they otherwise had the right combination of properties.

A concise summary of our observations, with recommended design strategies, is given in Table 2. We hope that this work will help guide experimental efforts to synthesize MOFs with targeted thermal conductivities using the strategies outlined above. Ultimately, for MOFs to find practical industrial use, they will need to possess not only great gas adsorption characteristics, but a myriad of other material properties important in chemical engineering processes, of which efficient thermal transport is just one.

**METHODS****Hypothetical MOF databases**

A prerequisite for large-scale screening is the access to large number of MOF structures. Over the past decade, several databases of hypothetical MOFs have been developed and screened<sup>66–72</sup>. The first of these databases, was created by Wilmer and coworkers and contained about 137,000 MOFs<sup>66</sup>. The

structures in this database were generated with no bias about the underlying topology using a bottom-up approach where new combinations of building blocks extracted from previously synthesized MOFs were sequentially snapped together until a MOF structure would emerge<sup>66</sup>. Although diverse with respect to textural properties (e.g., pore size, surface area), this database contained only six topologies (nets), with MOFs in the *pcu* (primitive cubic unit) topology making up about 90% of the database. To enforce topological diversity, codes using an alternative top-down approach where building blocks are snapped onto a topological template emerged in subsequent years. These include AuToGraFS by Addicoat et al.<sup>67</sup>, ToBaCCo by Boyd et al.<sup>68</sup>, and ToBaCCo by Gomez-Gualdrón et al.<sup>69</sup>. With the latter code, a  $\sim 13,000$ -MOF database was created featuring 41 topologies. However, all the 41 topologies corresponded to edge transitive nets whose topological templates scale up (or down) isotropically when resized to match the size of the building blocks to be mapped onto them. The practical implication of this constraint was that only ‘single-linker’ MOFs featuring highly symmetric, low aspect-ratio linkers were generated, leaving vast extensive regions of the MOF design space unexplored.

To overcome the above constraint, some of us modified the ToBaCCo code to create a 3.0 version whose template scaling procedure occurred in the graph space instead of the Euclidian space, in practice providing access to MOF generation in the more than 2800 non-edge transitive topologies known to date<sup>50,73</sup>. To date, more than to generate a proper database, ToBaCCo-3.0 have been used to generate versatile MOF sets to satisfy the needs of a given study<sup>51,74,75</sup>. For the present work, ToBaCCo-3.0 was used to create a topologically diverse set of 10,194 hypothetical MOFs featuring 1015 topologies, 24 metal-based nodular building blocks, 14 organic nodular building blocks and 40 organic edge building blocks. As the name suggests, nodular and edge building blocks (metal-based or organic) are mapped onto the nodes and edges of the topological template, where an edge is the line drawn between two connected nodes. What synthetic chemists would refer as the MOF secondary building units (SBUs) essentially correspond to the metal-based nodular building blocks. What synthetic chemists would refer as the organic linker essentially correspond to either edge building blocks or a combination of edge and organic nodular building blocks.

**Molecular dynamics simulation and Green-Kubo method**

For predicting thermal conductivities, we used equilibrium molecular dynamics simulations and the Green-Kubo formulation, which is based on the fluctuation-dissipation theorem<sup>76</sup>, and describe the thermal conductivity element  $k_{ii}$  of the thermal

conductivity tensor as<sup>77</sup>:

$$k_{ii} = \frac{V}{k_b T^2} \int_0^\infty \langle J_i(t) J_i(0) \rangle dt, i = x, y, z. \quad (1)$$

In Eq. 1,  $V$  is the volume of the simulation cell,  $T$  is temperature, and  $k_b$  is the Boltzmann constant.  $\langle J_i(t) J_i(0) \rangle$  is the heat current autocorrelation function (HCACF), which shows how strong the correlation is between heat fluxes at time zero and  $t$ . The HCACF is integrated over a chosen correlation time to calculate the value of the  $i$ -th diagonal element of the thermal conductivity tensor. We implicitly assumed that electrons do not contribute to thermal conductivity and made sure that the simulation cell was larger than 30 Å in each dimension to minimize finite-size effects<sup>76</sup>.

For sufficient sampling of the phase space, we averaged eight independent simulations, each of which had a different initial velocity distribution (seed), to calculate the thermal conductivity for each MOF structure. In each simulation, we calculated the thermal conductivity for each of the  $x$ -,  $y$ -, and  $z$ - directions and averaged them to obtain the average thermal conductivity values, except when considering anisotropic thermal transport properties. Thus, each MOF's directional and average thermal conductivities are the averages of 8 and 24 independent directional thermal conductivity values, respectively. The effect of the number of simulations used on the thermal conductivity is discussed in more detail in Supplementary Methods.

All calculations were performed using the molecular dynamics package LAMMPS<sup>78</sup>. We used the version of LAMMPS that has implemented the corrected heat flux calculations for many-body terms<sup>79</sup>. We chose a timestep of 0.5 fs across all structures. Initially, we used the  $NVT$  (canonical constant-volume-constant-temperature) ensemble for 500 ps at 300 K to set the temperature. After that, structures were equilibrated using the  $NVE$  (microcanonical constant-volume-constant-energy) ensemble for 100 ps followed by a final  $NVE$  production run for 500 ps. During the production run, we calculated the HCACF every five timesteps. To describe bonded intramolecular interactions between MOF framework atoms, we used the extension of the Universal Force Field (UFF)<sup>80</sup> developed for MOFs (UFF4MOF)<sup>81</sup>. Non-bonded van der Waals interactions were computed with a cut-off radius of 12.5 Å, whereas electrostatic interactions were not included due to the high computational cost.

### The adaptive averaging algorithm

Mean thermal conductivity is extracted from the HCACF data by averaging instantaneous thermal conductivity values over certain correlation time intervals, namely where the thermal conductivity values plateau. Plots of instantaneous thermal conductivity versus correlation time are shown in Supplementary Fig. 6. For some MOFs, we observed non-decaying oscillatory behavior (Supplementary Fig. 6b). In these cases, since oscillations showed very high amplitude that did not decay appreciably over the correlation times considered, extracting a mean thermal conductivity value was difficult. Thus, when choosing a fitting region, we considered the average amplitude of the oscillations in addition to the slope of the linear fit. Due to the large number of MOFs that we screened, we automated the extraction of thermal conductivity values by developing an algorithm that adaptively determined the appropriate plateaued interval based on a set of criteria. The search strategy we implemented for finding the optimal plateaued interval was to iteratively perform linear fitting to data segments of 2 ps in length at 1 ps increments, if the data was between 0 and 10 ps, and segments of 10 ps length at 5 ps increments if the data was beyond 10 ps. Then we calculated normalized slopes and the normalized average oscillation amplitudes with respect to the average thermal conductivity for each of those data segments. Finally, the algorithm considers the 0–10 ps correlation time window to check if any linear segment has a normalized average amplitude and normalized slope that is

less than 0.5 and 0.01 ps<sup>-1</sup>, respectively. If a single data segment satisfied the criteria, we accepted that interval. If there were multiple segments that satisfied the criteria, we sorted them based on the normalized amplitude and looked at the normalized slope for the segment with the lowest normalized amplitude if it meets the criteria. If we could not find any suitable plateaued interval within the 0–10 ps window, we moved to the correlation window between 10 and 50 ps and repeated the above-described search algorithm. We first considered the correlation time interval of 0–10 ps because most MOFs generally converge before 10 ps, and typically MOFs tend to have low thermal conductivities, which might show up at the beginning of the correlation time. The additional details are explained in the Supplementary Methods.

### Calculation of structural properties

Surface area was geometrically calculated by rolling a nitrogen-sized ( $\sigma = 3.71$  Å) spherical probe on MOF atoms. The surface area corresponded to the area of the surface traced by the center of the probe<sup>82</sup>. Void fractions were calculated using the Widom insertion method with a helium atom as probe ( $\sigma = 2.64$  Å,  $\epsilon/K = 10.9$ )<sup>83</sup>. Largest and limiting pore diameters (LPD and PLD, respectively) were calculated using Zeo++ (version 0.2.2)<sup>84</sup>.

### DATA AVAILABILITY

All 10,194 hypothetical MOF structures in a CIF file format are available at: <https://github.com/meirbek-islamov/thermal-transport-MOFs>.

### CODE AVAILABILITY

The ToBaCCo –3.0 code used to generate hypothetical MOF structures are described and referenced in the “Methods” section and is publicly available.

Received: 22 September 2022; Accepted: 22 December 2022;

Published online: 20 January 2023

### REFERENCES

- Kitagawa, S., Kitaura, R. & Noro, S. Functional porous coordination polymers. *Angew. Chem. Int. Ed.* **43**, 2334–2375 (2004).
- Rowsell, J. L. C. & Yaghi, O. M. Metal–organic frameworks: a new class of porous materials. *Microporous Mesoporous Mater.* **73**, 3–14 (2004).
- Rosi, N. L. Hydrogen storage in microporous metal–organic frameworks. *Science*. **300**, 1127–1129 (2003).
- Furukawa, H., Cordova, K. E., O’Keeffe, M. & Yaghi, O. M. The chemistry and applications of metal–organic frameworks. *Science*. **341**, 1230444 (2013).
- Mason, J. A., Veenstra, M. & Long, J. R. Evaluating metal–organic frameworks for natural gas storage. *Chem. Sci.* **5**, 32–51 (2014).
- He, Y., Zhou, W., Qian, G. & Chen, B. Methane storage in metal–organic frameworks. *Chem. Soc. Rev.* **43**, 5657–5678 (2014).
- Sumida, K. et al. Carbon dioxide capture in metal–organic frameworks. *Chem. Rev.* **112**, 724–781 (2012).
- Matsuda, R. et al. Highly controlled acetylene accommodation in a metal–organic microporous material. *Nature* **436**, 238–241 (2005).
- Li, J.-R., Kuppler, R. J. & Zhou, H.-C. Selective gas adsorption and separation in metal–organic frameworks. *Chem. Soc. Rev.* **38**, 1477 (2009).
- Qiu, S., Xue, M. & Zhu, G. Metal–organic framework membranes: from synthesis to separation application. *Chem. Soc. Rev.* **43**, 6116–6140 (2014).
- Seo, J. S. et al. A homochiral metal–organic porous material for enantioselective separation and catalysis. *Nature*. **404**, 982–986 (2000).
- Allendorf, M. D. et al. Stress-induced chemical detection using flexible metal–organic frameworks. *J. Am. Chem. Soc.* **130**, 14404–14405 (2008).
- Kreno, L. E. et al. Metal–organic framework materials as chemical sensors. *Chem. Rev.* **112**, 1105–1125 (2012).
- Hu, Z., Deibert, B. J. & Li, J. Luminescent metal–organic frameworks for chemical sensing and explosive detection. *Chem. Soc. Rev.* **43**, 5815–5840 (2014).
- Lee, J. et al. Metal–organic framework materials as catalysts. *Chem. Soc. Rev.* **38**, 1450 (2009).

16. Liu, J. et al. Applications of metal–organic frameworks in heterogeneous supra-molecular catalysis. *Chem. Soc. Rev.* **43**, 6011–6061 (2014).
17. Zhang, T. & Lin, W. Metal–organic frameworks for artificial photosynthesis and photocatalysis. *Chem. Soc. Rev.* **43**, 5982–5993 (2014).
18. Horcajada, P. et al. Porous metal–organic-framework nanoscale carriers as a potential platform for drug delivery and imaging. *Nat. Mater.* **9**, 172–178 (2010).
19. Faust, T. MOFs deliver. *Nat. Chem.* **7**, 270–271 (2015).
20. Teplensky, M. H. et al. Temperature treatment of highly porous zirconium-containing metal–organic frameworks extends drug delivery release. *J. Am. Chem. Soc.* **139**, 7522–7532 (2017).
21. Sun, L. et al. A microporous and naturally nanostructured thermoelectric metal–organic framework with ultralow thermal conductivity. *Joule*. **1**, 168–177 (2017).
22. Erickson, K. J. et al. Thin film thermoelectric metal–organic framework with high seebeck coefficient and low thermal conductivity. *Adv. Mater.* **27**, 3453–3459 (2015).
23. Jin, H. et al. Hybrid organic–inorganic thermoelectric materials and devices. *Angew. Chem. Int. Ed.* **58**, 15206–15226 (2019).
24. Redel, E. & Baumgart, H. Thermoelectric porous MOF based hybrid materials. *APL Mater.* **8**, 060902 (2020).
25. Fan, Y., Liu, Z. & Chen, G. Recent progress in designing thermoelectric metal–organic frameworks. *Small*. **17**, 2100505 (2021).
26. Furukawa, H. et al. Ultrahigh porosity in metal–organic frameworks. *Science*. **329**, 424–428 (2010).
27. Materials Design and Discovery Group. et al. A route to high surface area, porosity and inclusion of large molecules in crystals. *Nature*. **427**, 523–527 (2004).
28. Zheng, Q., Hao, M., Miao, R., Schaadt, J. & Dames, C. Advances in thermal conductivity for energy applications: a review. *Prog. Energy*. **3**, 012002 (2021).
29. Makal, T. A., Li, J.-R., Lu, W. & Zhou, H.-C. Methane storage in advanced porous materials. *Chem. Soc. Rev.* **41**, 7761 (2012).
30. Huang, B. L., McGaughey, A. J. H. & Kaviani, M. Thermal conductivity of metal–organic framework 5 (MOF-5): Part I. Molecular dynamics simulations. *Int. J. Heat. Mass Transf.* **50**, 393–404 (2007).
31. Huang, B. L. et al. Thermal conductivity of a metal–organic framework (MOF-5): Part II. Measurement. *Int. J. Heat. Mass Transf.* **50**, 405–411 (2007).
32. Liu, D. et al. MOF-5 composites exhibiting improved thermal conductivity. *Int. J. Hydrog. Energy* **37**, 6109–6117 (2012).
33. Wang, X. et al. Anisotropic Lattice Thermal Conductivity and Suppressed Acoustic Phonons in MOF-74 from First Principles. *J. Phys. Chem. C*. **119**, 26000–26008 (2015).
34. Babaei, H., McGaughey, A. J. H. & Wilmer, C. E. Transient mass and thermal transport during methane adsorption into the metal–organic framework HKUST-1. *ACS Appl. Mater. Interfaces* **10**, 2400–2406 (2018).
35. Sezginel, K. B., Lee, S., Babaei, H. & Wilmer, C. E. Effect of flexibility on thermal transport in breathing porous crystals. *J. Phys. Chem. C*. **124**, 18604–18608 (2020).
36. Babaei, H. et al. Observation of reduced thermal conductivity in a metal–organic framework due to the presence of adsorbates. *Nat. Commun.* **11**, 4010 (2020).
37. Babaei, H., McGaughey, A. J. H. & Wilmer, C. E. Effect of pore size and shape on the thermal conductivity of metal–organic frameworks. *Chem. Sci.* **8**, 583–589 (2017).
38. Sezginel, K. B., Asinger, P. A., Babaei, H. & Wilmer, C. E. Thermal transport in interpenetrated metal–organic frameworks. *Chem. Mater.* **30**, 2281–2286 (2018).
39. Islamov, M., Babaei, H. & Wilmer, C. E. Influence of missing linker defects on the thermal conductivity of metal–organic framework HKUST-1. *ACS Appl. Mater. Interfaces* **12**, 56172–56177 (2020).
40. Babaei, H. & Wilmer, C. E. Mechanisms of heat transfer in porous crystals containing adsorbed gases: applications to metal–organic frameworks. *Phys. Rev. Lett.* **116**, 025902 (2016).
41. Babaei, H., Lee, J.-H., Dods, M. N., Wilmer, C. E. & Long, J. R. Enhanced thermal conductivity in a diamine-appended metal–organic framework as a result of cooperative CO<sub>2</sub> adsorption. *ACS Appl. Mater. Interfaces*. **12**, 44617–44621 (2020).
42. Ying, P., Zhang, J., Zhang, X. & Zhong, Z. Impacts of functional group substitution and pressure on the thermal conductivity of ZIF-8. *J. Phys. Chem. C*. **124**, 6274–6283 (2020).
43. Wieser, S. et al. Identifying the bottleneck for heat transport in metal–organic frameworks. *Adv. Theory Simul.* **4**, 2000211 (2021).
44. Huang, J., Xia, X., Hu, X., Li, S. & Liu, K. A general method for measuring the thermal conductivity of MOF crystals. *Int. J. Heat. Mass Transf.* **138**, 11–16 (2019).
45. Chae, J. et al. Nanophotonic atomic force microscope transducers enable chemical composition and thermal conductivity measurements at the nanoscale. *Nano Lett.* **17**, 5587–5594 (2017).
46. Cui, B. et al. Thermal conductivity of ZIF-8 thin-film under ambient gas pressure. *ACS Appl. Mater. Interfaces* **9**, 28139–28143 (2017).
47. Gunatilleke, W. D. C. B. et al. Thermal conductivity of a perovskite-type metal–organic framework crystal. *Dalton Trans.* **46**, 13342–13344 (2017).
48. Cheng, R., Li, W., Wei, W., Huang, J. & Li, S. Molecular insights into the correlation between microstructure and thermal conductivity of zeolitic imidazolate frameworks. *ACS Appl. Mater. Interfaces* **13**, 14141–14149 (2021).
49. Han, L., Budge, M. & Alex Greaney, P. Relationship between thermal conductivity and framework architecture in MOF-5. *Comput. Mater. Sci.* **94**, 292–297 (2014).
50. Anderson, R. & Gómez-Gualdrón, D. A. Increasing topological diversity during computational “synthesis” of porous crystals: how and why. *Cryst. Eng. Comm.* **21**, 1653–1665 (2019).
51. Anderson, R. & Gómez-Gualdrón, D. A. Large-scale free energy calculations on a computational metal–organic frameworks database: toward synthetic likelihood predictions. *Chem. Mater.* **32**, 8106–8119 (2020).
52. Wieme, J. et al. Thermal engineering of metal–organic frameworks for adsorption applications: a molecular simulation perspective. *ACS Appl. Mater. Interfaces* **11**, 38697–38707 (2019).
53. Chen, Z. et al. Balancing volumetric and gravimetric uptake in highly porous materials for clean energy. *Science*. **368**, 297–303 (2020).
54. Graebner, J. E. Thermal conductivity of diamond. In *Diamond: Electronic Properties and Applications* (eds. Pan, L. S. & Kania, D. R.) 285–318 (Springer US, 1995).
55. Kang, J. S., Li, M., Wu, H., Nguyen, H. & Hu, Y. Experimental observation of high thermal conductivity in boron arsenide. *Science*. **361**, 575–578 (2018).
56. Qian, X., Zhou, J. & Chen, G. Phonon-engineered extreme thermal conductivity materials. *Nat. Mater.* **20**, 1188–1202 (2021).
57. Duda, J. C., Hopkins, P. E., Shen, Y. & Gupta, M. C. Exceptionally low thermal conductivities of films of the fullerene derivative PCBM. *Phys. Rev. Lett.* **110**, 015902 (2013).
58. Moghadam, P. Z. et al. Structure–mechanical stability relations of metal–organic frameworks via. *Mach. Learn. Matter.* **1**, 219–234 (2019).
59. Goodson, K. E. Ordering up the minimum thermal conductivity of solids. *Science*. **315**, 342–343 (2007).
60. Blakemore, J. S. Semiconducting and other major properties of gallium arsenide. *J. Appl. Phys.* **53**, R123–R181 (1982).
61. Ma, H., Aamer, Z. & Tian, Z. Ultrahigh thermal conductivity in three-dimensional covalent organic frameworks. *Mater. Today Phys.* **21**, 100536 (2021).
62. Giri, A., Dionne, C. J. & Hopkins, P. E. Atomic coordination dictates vibrational characteristics and thermal conductivity in amorphous carbon. *npj Comput. Mater.* **8**, 55 (2022).
63. Henry, A. & Chen, G. High thermal conductivity of single polyethylene chains using molecular dynamics simulations. *Phys. Rev. Lett.* **101**, 235502 (2008).
64. Shen, S., Henry, A., Tong, J., Zheng, R. & Chen, G. Polyethylene nanofibres with very high thermal conductivities. *Nat. Nanotechnol.* **5**, 251–255 (2010).
65. Morelli, D. T., Heremans, J., Sakamoto, M. & Uher, C. Anisotropic heat conduction in diacetylenes. *Phys. Rev. Lett.* **57**, 869–872 (1986).
66. Wilmer, C. E. et al. Large-scale screening of hypothetical metal–organic frameworks. *Nat. Chem.* **4**, 83–89 (2012).
67. Addicoat, M. A., Coupry, D. E. & Heine, T. AuToGraFS: automatic topological generator for framework structures. *J. Phys. Chem. A* **118**, 9607–9614 (2014).
68. Boyd, P. G. & Woo, T. K. A generalized method for constructing hypothetical nanoporous materials of any net topology from graph theory. *Cryst. Eng. Comm.* **18**, 3777–3792 (2016).
69. Gómez-Gualdrón, D. A. et al. Evaluating topologically diverse metal–organic frameworks for cryo-adsorbed hydrogen storage. *Energy Environ. Sci.* **9**, 3279–3289 (2016).
70. Groom, C. R., Bruno, I. J., Lightfoot, M. P. & Ward, S. C. The Cambridge Structural Database. *Acta Crystallogr. B. Struct. Sci. Cryst. Eng. Mater.* **72**, 171–179 (2016).
71. Boyd, P. G. et al. Data-driven design of metal–organic frameworks for wet flue gas CO<sub>2</sub> capture. *Nature*. **576**, 253–256 (2019).
72. Colón, Y. J., Gómez-Gualdrón, D. A. & Snurr, R. Q. Topologically guided, automated construction of metal–organic frameworks and their evaluation for energy-related applications. *Cryst. Growth Des.* **17**, 5801–5810 (2017).
73. O’Keeffe, M., Peskov, M. A., Ramsden, S. J. & Yaghi, O. M. The reticular chemistry structure resource (RCSR) database of, and symbols for, crystal nets. *Acc. Chem. Res.* **41**, 1782–1789 (2008).
74. Anderson, R., Rodgers, J., Argueta, E., Biong, A. & Gómez-Gualdrón, D. A. Role of pore chemistry and topology in the CO<sub>2</sub> capture capabilities of MOFs: from molecular simulation to machine learning. *Chem. Mater.* **30**, 6325–6337 (2018).
75. Anderson, R., Biong, A. & Gómez-Gualdrón, D. A. Adsorption isotherm predictions for multiple molecules in MOFs using the same deep learning model. *J. Chem. Theory Comput.* **16**, 1271–1283 (2020).
76. Sellan, D. P., Landry, E. S., Turney, J. E., McGaughey, A. J. H. & Amon, C. H. Size effects in molecular dynamics thermal conductivity predictions. *Phys. Rev. B* **81**, 214305 (2010).
77. Babaei, H., Keblinski, P. & Khodadadi, J. M. Equilibrium molecular dynamics determination of thermal conductivity for multi-component systems. *J. Appl. Phys.* **112**, 054310 (2012).
78. Plimpton, S. Fast parallel algorithms for short-range molecular dynamics. *J. Comput. Phys.* **117**, 1–19 (1995).

79. Boone, P., Babaei, H. & Wilmer, C. E. Heat flux for many-body interactions: corrections to LAMMPS. *J. Chem. Theory Comput.* **15**, 5579–5587 (2019).
80. Rappe, A. K., Casewit, C. J., Colwell, K. S., Goddard, W. A. & Skiff, W. M. UFF, a full periodic table force field for molecular mechanics and molecular dynamics simulations. *J. Am. Chem. Soc.* **114**, 10024–10035 (1992).
81. Coupry, D. E., Addicoat, M. A. & Heine, T. Extension of the universal force field for metal–organic frameworks. *J. Chem. Theory Comput.* **12**, 5215–5225 (2016).
82. Gómez-Gualdrón, D. A., Moghadam, P. Z., Hupp, J. T., Farha, O. K. & Snurr, R. Q. Application of consistency criteria to calculate BET areas of micro- and mesoporous metal–organic frameworks. *J. Am. Chem. Soc.* **138**, 215–224 (2016).
83. Talu, O. & Myers, A. L. Molecular simulation of adsorption: gibbs dividing surface and comparison with experiment. *AIChE J.* **47**, 1160–1168 (2001).
84. Willems, T. F., Rycroft, C. H., Kazi, M., Meza, J. C. & Haranczyk, M. Algorithms and tools for high-throughput geometry-based analysis of crystalline porous materials. *Microporous Mesoporous Mater.* **149**, 134–141 (2012).

## ACKNOWLEDGEMENTS

M.I. and C.E.W. gratefully acknowledge support from the National Science Foundation (NSF), awards CBET- 1804011 and OAC-1931436, and also thank the Center for Research Computing (CRC) at the University of Pittsburgh for providing computational resources. D.A.G.-G. acknowledges funding from the Institute from Data-Driven Dynamical Design (ID4) funded through NSF grant OAC-2118201 and also thanks access to the Mio supercomputer at Colorado School of Mines. A.J.H.M acknowledges funding from the National Science Foundation (NSF), award DMR-2025013. H.B. and J.R.L. gratefully acknowledge support from the Hydrogen Materials - Advanced Research Consortium (HyMARC), established as part of the Energy Materials Network under the U.S. Department of Energy, Office of Energy Efficiency and Renewable Energy, under Contract No. DE-AC02-05CH11231.

## AUTHOR CONTRIBUTIONS

M.I. performed the simulations, analyzed the results, and wrote the manuscript. R.A. and D.A.G.-G. generated the hypothetical MOF structures and calculated their textural properties. H.B., K.B.S., J.R.L., A.J.H.M., and D.A.G.-G. contributed to the discussion of the project. C.E.W. supervised the research and contributed to the revision of the

manuscript. All authors reviewed and edited the manuscript.

## COMPETING INTERESTS

C.E.W. declares no competing non-financial interests but the following competing financial interests: C.E.W. has start-up company NuMat Technologies, which is seeking to commercialize metal–organic frameworks. All other authors declare there is no competing interests.

## ADDITIONAL INFORMATION

**Supplementary information** The online version contains supplementary material available at <https://doi.org/10.1038/s41524-022-00961-x>.

**Correspondence** and requests for materials should be addressed to Hasan Babaei or Christopher E. Wilmer.

**Reprints and permission information** is available at <http://www.nature.com/reprints>

**Publisher's note** Springer Nature remains neutral with regard to jurisdictional claims in published maps and institutional affiliations.



**Open Access** This article is licensed under a Creative Commons Attribution 4.0 International License, which permits use, sharing, adaptation, distribution and reproduction in any medium or format, as long as you give appropriate credit to the original author(s) and the source, provide a link to the Creative Commons license, and indicate if changes were made. The images or other third party material in this article are included in the article's Creative Commons license, unless indicated otherwise in a credit line to the material. If material is not included in the article's Creative Commons license and your intended use is not permitted by statutory regulation or exceeds the permitted use, you will need to obtain permission directly from the copyright holder. To view a copy of this license, visit <http://creativecommons.org/licenses/by/4.0/>.

© The Author(s) 2023